Title

Full title: From Initial Formation to Developmental Refinement: GABAergic Inputs Shape Neuronal Subnetworks in the Primary Somatosensory Cortex

- Short title: The refinement of neuronal subnetwork

Authors

Jui-Yen Huang[1-3*], Michael Hess[1#], Abhinav Bajpai[4], Xuan Li[1-2], Liam N Hobson[1-2], Ashley J Xu[1-3], Scott J Barton[1-2], Hui-Chen Lu[1-3*]

Affiliations

[1]The Gill Institute for Neuroscience, Indiana University, Bloomington, IN 47405.

[2]Department of Psychological and Brain Sciences, Indiana University, Bloomington, IN 47405.

[3]Program in Neuroscience, Indiana University, Bloomington, IN 47405.

[4]Research Technologies, Indiana University Bloomington, IN 47408.

[#]Current address: Neuroscience Graduate Program, Emory University, Atlanta 30322

Corresponding Authors and Addresses:

Hui-Chen Lu, Ph.D.

Gill Institute for Neuroscience and Department of Psychological and Brain Sciences

Indiana University

702 N Walnut Grove Ave

Bloomington, IN 47405

Tel: 812-856-4998

Fax: 812-856-7187

Email: hclu@iu.edu

Jui-Yen Huang, Ph.D.

Gill Institute for Neuroscience and Department of Psychological and Brain Sciences

Indiana University

702 N Walnut Grove Ave

Bloomington, IN 47405

Tel: 812-856-5152

Fax: 812-856-7187

Email: juiyhuan@iu.edu

Abstract

Neuronal subnetworks, also known as ensembles, are functional units formed by interconnected neurons for information processing and encoding in the adult brain. Our study investigates the establishment of neuronal subnetworks in the mouse primary somatosensory (S1) cortex from postnatal days (P)11 to P21 using *in vivo* two-photon calcium imaging. We found that at P11, neuronal activity was highly synchronized but became sparser by P21. Clustering analyses revealed that while the number of subnetworks remained constant, their activity patterns became more distinct, with increased coherence, independent of cortical layer or sex. Furthermore, the coherence of neuronal activity within individual subnetworks significantly increased when synchrony frequencies were reduced by augmenting GABAergic activity at P15/16, a period when the neuronal subnetworks were still maturing. Together, these findings indicate the early formation of subnetworks and underscore the pivotal roles of GABAergic inputs in modulating S1 neuronal subnetworks.

Teaser

Utilizing clustering algorithms to reveal the principles governing cortical subnetwork assembly in the developing brain.

Introduction

For the brain to perform complex information processing, its circuits organize into small functional units called subnetworks or ensembles. Neurons in the same subnetwork exhibit recurrent coordinated activity and are consistently recruited by specific sensory stimuli, motor programs, or cognitive states (*1-9*). Several studies have shown that neurons from different subnetworks, encoding different types of information, are spatially intermingled and distributed across large brain volumes (*1, 2, 4, 7*). Despite their wide topographical distribution, neurons within each subnetwork also co-activate with activity patterns that resemble externally evoked activity patterns when external inputs are weak or absent (*8, 10-12*). These findings suggest that a subnetwork is a pre-configured functional unit ready to receive or integrate information input. Currently, it is unclear when such functional subnetworks assemble, and what factors refine their functional connectivity during brain development.

Two-photon calcium imaging has been used to visualize neuronal activity at population levels in the developing brain (*13-22*). These studies typically evaluated activity patterns with two metrics: synchrony frequency, which measures the simultaneous burst activation of neurons, and the Pearson correlation coefficient, which quantifies the degree of correlated activity between neuron pairs (*15, 17-20*). During the first postnatal week, both glutamatergic and GABAergic neurons in the developing rodent primary somatosensory cortex (S1) exhibit high levels of synchronization and correlation (*15-22*). Three distinct phases of activity patterns have been identified in S1 layer (L) 4 neurons during postnatal day (P)1 to P11: patchwork-type (P1-P7), synchronized (P7-P11), and sparse (after P11) (*15, 17*). From P11 to P21, L2/3 neurons exhibit highly synchronous and correlated activation patterns before transitioning to sparser patterns (*18, 19, 21, 23*).

During this postnatal period, particularly after P7, both excitatory and inhibitory circuits in S1 cortex become more established and acquire greater strength (*24-27*). Around P9, recurrent excitatory connectivity in L4 glutamatergic neurons increases (*26, 27*), while the number of inhibitory synapses on glutamatergic neurons gradually rises from P9 to P28 (*24, 25*). Between P10 and P20, the frequency of spontaneous inhibitory postsynaptic currents (sIPSCs) in L2/3 excitatory neurons increases, while the frequency of spontaneous excitatory postsynaptic currents (sEPSCs) decreases (*25*), suggesting that inhibition increases more than excitation. Given that the maturation of gamma-aminobutyric acid (GABA)ergic neurons aligns with the desynchronization of population

activity, we hypothesized that increasing inhibitory inputs contribute to the transition from synchronized activity to sparse coding, thereby influencing subnetwork assembly in the S1 cortex.

In this study, we aimed to investigate the timing and mechanisms of S1 cortical neuron subnetwork assembly and explore the role of GABAergic inputs on subnetwork refinement. Using two-photon calcium imaging, we monitored the activity of S1 upper cortical layer (L2-4) neurons in awake neonatal mice from P11-P21. To identify neuronal subnetworks, we applied several clustering algorithms, including k-means clustering and a community detection method (*11, 16*), to find neurons with similar activity patterns and group them into subnetwork. Clustering analyses indicated the presence of neuronal subnetworks from the earliest postnatal age we imaged. Notably, the cohesiveness of activity within these subnetworks increased significantly from P11 to P21, regardless of cortical layer or sex. These findings highlight the early assembly of S1 neuronal subnetworks and the subsequent refinement in enhancing subnetwork coherence. Artificially enhanced GABAergic neuronal activity at P15/P16 resulted in reduced synchrony frequency and increased subnetwork coherence., This provides strong support for the contribution of GABAergic transmission in subnetwork maturation.

Results

Spontaneous neuronal activity decreased and desynchronized in both L2/3 and L4, irrespective of sex, from P11 to P21

To elucidate when S1 neuronal subnetworks assemble during postnatal brain development, we conducted *in vivo* two-photon calcium imaging with the red calcium sensor jRGECO1a to monitor neuronal activity in awake-behaving mouse pups. We injected an AAV carrying jRGECO1a into S1 at P1-P2 via stereotaxic intracranial injections and installed a cranial window at P8-P9 (Fig. 1A, Fig. S1A-B). We imaged pups in a head-restrained configuration (Fig. S1C-D) at P11, P13, P15, P18, and P21. Sequential imaging of a 505 x 505 μm field at different cortical depths was conducted to capture neuronal activity in the upper S1 cortical layers, L2/3 and L4. The cranial window installed on P8-9 cleared within two days and remained so until the final imaging day, P21 (Fig. 1B, Fig. S1F upper panel). Guided by vasculature patterns, we imaged the same cortical areas over the whole imaging period (Fig. S1F lower panel).

Raw calcium imaging datasets were preprocessed using Suite2P and FISSA for movement and neuropil correction, followed by the detection of calcium transients to estimate neuronal firing rates (Fig. S2A-D, see detailed description in Materials and Methods). To reveal cortical activity during the default mode, we employed cameras to simultaneously record body and facial movements of the mouse during calcium imaging. This allowed us to identify periods when the mouse pups were in a quiescence status, with minimal body movement, for subsequent calcium data analysis (Fig. S2E). Given the nested nature of the experimental design (*28-30*), such as imaging the same mice multiple times, we primarily employed linear mixed-effects (LME) models for multilevel statistical analysis (*31*). In cases where the data did not exhibit nesting, we used linear regression (LM) models to assess statistical significance instead (see Materials and Methods).

To investigate sex- or layer-dependent effects on spontaneous neuronal activity during cortical development, we first compared data from P11 and P21 for males and females in both L2/3 and L4. We observed a notable developmental decline in event frequency from P11 to P21 in L2/3 and L4, a consistent trend in both sexes (Fig. 1C, D). To quantify overall network activity, we computed synchrony events (Fig. 1E; see Materials and Methods). The results showed a significant decrease in synchrony frequency by P21, regardless of cortical layer or sex (Fig. 1F). We also quantified the correlated activity between neuronal pairs by calculating the Pearson correlation coefficient of normalized fluorescent traces from all neuronal pairs (Fig. S2F). Our analysis revealed a significant decrease in the mean correlation coefficient at P21 in L2/3 for both females and males. In In L4, females exhibited a significant decrease in the mean correlation coefficient from P11 to P21, while males did not (Fig. S2F). Furthermore, L2/3 neurons showed higher correlated activity compared to L4 neurons at P11, regardless of sex (Fig. S2F).

Taken together, our developmental studies with calcium imaging reveal that spontaneous neuronal activity decreased and became desynchronized in both L2/3 and L4 cortical neurons from P11 to P21, irrespective of sex. While overall activity patterns showed a consistent decrease and desynchronization, subtle differences in the extent and nature of correlated activity varied by sex and cortical layer.

Subnetworks are formed by P11 and become matured at P21 with increased coherence in activity patterns

We next asked when do cortical neuronal subnetworks form between P11 and P21. To find neurons exhibiting similar activity patterns, we employed an unsupervised k-means clustering algorithm (*11, 16*). This algorithm clustered the similarity matrix (covariance matrix) generated from frame-by-frame analysis of calcium events (Fig. S3A-B). Subsequently, neurons were assigned to the activity event cluster to which they made the greatest contribution, thereby revealing the neuronal subnetwork (Fig. 2A-C; see Materials and Methods).

To evaluate the quality of event clusters, we inspected the silhouette value (Fig. 2D), which serves as a metric for evaluating the similarity of a point to its own cluster (cohesion) and individuality compared to other clusters (separation). In other words, a higher silhouette value indicates greater similarity to other members within the same cluster and/or lower similarity to members of other clusters. After assigning neurons to the activity clusters to which they contributed most significantly (Fig. 2B-C), we found that neuronal subnetworks were already present at P11 and that similar numbers of subnetworks were found at P21 (Fig. 2E). Interestingly, our data analysis revealed a substantial increase in silhouette value from P11 to P21, spanning both cortical layers and sexes (Fig. 2D).

To validate the efficacy of K-means clustering algorithm in revealing subnetworks, we computed the tetrachoric correlation coefficient (tCC)—a suitable measure for binary data analogous to the Pearson correlation coefficient (*32*)— for all neuronal pairs, regardless of their subnetwork identities. This analysis involved calculating the tCC for both neuronal pairs within their specific subnetworks (inside) and pairwise for neurons between subnetworks (outside). Notably, the tCC of neuronal pairs within the same subnetworks at P11 and P21 was consistently higher than that of pairwise comparisons between neurons from different subnetworks (Fig. S3C). These results demonstrate the robustness of the clustering algorithm in grouping neurons based on the similarity of their activity patterns. Additionally, we observed that L2/3 neurons had a significantly heightened tCC at P21 compared to P11, regardless of sex (Fig. 2F), while a similar trend was observed in L4 neurons without reaching statistically significant ($p = 0.057$). It is possible that varying the number of neurons and time intervals in the analysis could influence the identification of subnetworks. To investigate this, we examined the correlations between the number of neurons included in the clustering analysis and the number of identified subnetworks (Spearman correlation coefficient, $\rho = -0.063$) (Fig. S3D). We also analyzed the

relationship between the time intervals used for clustering analysis and the number of subnetworks (Spearman correlation coefficient, $\rho = 0.233$) (Fig. S3E). These analyses conclude that both the number of neurons and time intervals have minimal impact on subnetwork identification.

Changes in subnetwork configuration and topographical distribution: a comparison between P11 and P21, from high participation to low and from segregation to intermingling

We next explored whether the higher correlated activity among neurons within the same subnetwork is maintained by removing neurons that exhibit lower correlated activity. We classified neurons based on their involvement in event clusters. For those participating in clusters, we examined whether they exclusively engaged in a single event cluster or were part of multiple event clusters. With these characteristics, neurons were separated into the following three categories: single-cluster neurons, non-cluster neurons, and multiple-cluster neurons. Our findings revealed a decrease in the percentage of single-cluster neurons with age (Fig. 3A), accompanied by a rise in the percentage of non-cluster neurons (Fig. 3B). The percentages of multiple-cluster neurons remained similar between P11 and P21 (Fig. 3C). This pattern of configuration was consistent across both L2/3 and L4 layers and between sexes (Fig. 3A-C).

Previous studies have demonstrated that neurons within the same subnetwork are spatially intermingled and distributed across large brain volumes in adult mice (*1, 2, 4*). Here we investigated the topographical distribution of each neuron based on their subnetwork identification and determined if their distribution patterns changed with age (Fig. 3D). To determine whether the physical size of neuronal subnetworks changes with age, we calculated the pairwise distance between neurons within the same cluster and the distance of each neuron to its cluster centroid. We found no significant differences between P11 and P21 in either measure within the same cortical layers (Fig. 3E, F). Interestingly, the pairwise distances between neurons and the distances from neurons to their subnetwork centroid were significantly greater in L4 neurons compared to L2/3 neurons at both P11 and P21, irrespective of sex (Fig. 3E, F). To evaluate the relative distributions among subnetworks, the pairwise distances between subnetwork centroids were quantitatively

compared. We observed a significant reduction in these distances from P11 to P21 for both cortical layer and sexes (Fig. 3G).

In summary, our results demonstrate that neuronal subnetworks in the S1 upper cortical layer are assembled as early as P11 and the number of subnetworks remains consistent between P11 and P21. Notably, by P21, these subnetworks exhibit greater coherence in activity patterns while having fewer neurons within each cluster. Additionally, the spatial distribution of these subnetworks evolves from initially segregated to more intermingled patterns.

The refinement of S1 neuronal subnetworks occurs during the 2nd to 3rd postnatal weeks

To examine the developmental trajectory of cortical subnetwork assembly, we analyzed imaging data acquired from age groups P11, P13, P15, P18, and P21, merging data from females and males when no sex-dependent effect was observed. We quantified the mean differences among age groups to reveal the developmental transition periods for individual network properties. A developmental decline in spontaneous neuronal event frequency was observed (Fig 4A), with the greatest mean difference occurring between P11 and P18 (Fig. 4A) while synchrony frequency showed a gradual decline from P11 to P21 (Fig. 4B). The pairwise correlation coefficient exhibited layer- and sex-dependent changes. Female L2/3 and L4 neurons showed a gradual decrease in their correlation coefficients during P11-P21 and P11-P18, respectively (Fig. S4A). In males, L2/3 and L4 neurons exhibited a gradual decline in pairwise correlation coefficients from P11 to P15, followed by a transient increase at P18.

With the subnetwork analysis, we found a transient but modest increase in the subnetwork number at P15 (Fig. 4C). For event cluster coherences, the silhouette value gradually increased from P11 to P21, regardless of sex and cortical layer (Fig. 4D). At P15, males transiently exhibited significantly higher silhouette values than females (Fig. 4D). Interestingly, as indicated by the tCC of neurons within the same subnetworks, L2/3 neurons reached their maximum subnetwork-based correlation earlier than L4 neurons: the maximum mean difference for L2/3 occurred at P15, while for L4 occurred at P18, regardless of sex (Fig. 4E). The developmental trajectory of subnetwork configuration showed that the percentage of single-cluster neurons gradually decreased from P11 to P18

248 (Fig. 4F), while the percentage of non-cluster neurons increased from P11 to P21 (Fig.
249 4G). The percentage of neurons participating in multiple clustering remained consistent
250 throughout the observation period (Fig. 4H).

251 Regarding the spatial distribution of subnetwork neurons, our analysis suggests that the
252 spatial distribution of subnetworks became more intermingled after P18. We found that
253 the maximum mean difference in physical size indices—specifically, the pairwise
254 distances between neurons and the distance of neurons to their subnetwork centroid—
255 occurred between P13 and P21, regardless of cortical layer or sex (Fig. S4B, C). Notably,
256 the pairwise distances between subnetwork centroids gradually decreased from P11 to
257 P21, with the largest reduction observed in L2/3 and L4 neurons during P11-P21 and P11-
258 P18, respectively (Fig. S4D).

259 In summary, our results demonstrate that nascent subnetworks undergo a dynamic
260 developmental transformation between P11 to P21. The coherences of neuronal activity
261 patterns, as indicated by increased silhouette values, is significantly enhanced during this
262 period. Interestingly, the number of neurons participating in a single subnetwork declines
263 with age. These data suggest that the 2nd to 3rd postnatal weeks are a critical period for
264 subnetwork development, with P15 serving as a particularly notable transition point.
265 During this developmental transition, cortical neurons intricately enhance their functional
266 connections and form highly correlated subnetworks that become increasingly
267 independent of other subnetworks.

268

269 **Acute GABAergic transmission augmentation increases the coherence of cortical**
270 **subnetworks**

271 Inhibitory inputs from GABAergic neurons in S1 cortex increase substantially from the
272 2nd to 3rd postnatal week (*24, 25*), matching the period we observed the developmental
273 transitions for various subnetwork properties. To investigate whether GABAergic inputs
274 play a role in refining S1 cortical subnetwork properties, we employed a designer receptor
275 exclusively activated by designer drugs (DREADD)-based approach to acutely enhance
276 GABAergic neuronal transmission (*33*). Specifically, we injected an AAV mixture of
277 synapsin-jRGECO1a and Dlx5/6-hM3Dq at P1-P2 and installed cranial windows at P8-P9
278 (Fig. 5A). We confirmed that the majority of jRGECO1a-expressing neurons were

279 glutamatergic neurons, while Dlx5/6-hM3Dq-positive neurons were predominantly
280 GABAergic (Fig. S5), as previously reported (*33*).

281 P15-P16, the midpoint of developmental transitions between P11-21, was selected for
282 assessing the impact of GABAergic input on neuronal subnetworks. After baseline
283 calcium imaging, we administered the hM3Dq ligand, clozapine-N-oxide (CNO; 1 mg/kg,
284 intraperitoneally), to enhance the excitability of GABAergic neurons (Fig. 5A). 30-60
285 minutes post-CNO treatment, calcium imaging was conducted to determine its impact.
286 This acute enhancement of GABAergic activity significantly reduced the frequency of
287 both individual calcium events (Fig. 5B, C) and synchronized events (Figure 5D), in both
288 L2/3 and L4 neurons, and across both sexes. Despite the substantial reduction in event
289 frequencies and synchronized events, CNO administration did not exhibit a detectable
290 impact on Pearson correlation coefficient of all neuronal pairs (Fig. S6A).

291 Results from subnetwork analysis showed that acute CNO treatment robustly increased
292 silhouette values of event clusters in both L2/3 and L4, independent of sex (Fig. 5E),
293 while keep the subnetwork numbers constant (Fig. S6B). The intensified tCC within the
294 same subnetwork due to acute GABAergic enhancement was particularly evident in
295 females for both L2/3 and L4 (Fig. S6C). Regarding the impact of GABAergic inputs on
296 subnetwork configurations, we observed that CNO treatment decreased the percentage of
297 single-cluster neurons (Fig. 5F) while increasing the percentage of multiple-cluster
298 neurons (Fig. 5H). The percentage of non-cluster neurons was not significantly altered by
299 CNO treatment (Fig. 5G). Analysis of the topographical distribution of neurons showed
300 that CNO application had no detectable impact on the distances between neurons within
301 the same subnetwork (Fig. S6D), the distance of individual neurons to their respective
302 subnetwork centroid (Fig. S6E), or the pairwise distances between subnetwork centroids
303 (Fig. S6F). Taken together, our data suggested that enhancing functional GABAergic
304 inputs increases the sparseness of neuronal activity and cortical subnetwork cohesiveness
305 without altering the anatomical distributions of the subnetworks.

306

307 **Discussion**

308 In this study, we examined the development of S1 cortical subnetworks by imaging
309 neuronal activity in both female and male mouse pups from P11 to P21, with a specific
310 focus on periods of behavioral quiescence. Through the application of multiple clustering

algorithms and rigorous statistical methods, including multilevel analysis with bootstrapping, we ensured the robustness of our findings. Our results reveal that cortical subnetworks are already present by P11, the earliest time point we assessed, and the number of subnetworks remains relatively stable from P11 to P21. However, these early networks undergo significant refinement with an increase in the cohesiveness of activity patterns within individual subnetworks, alongside a better distinction among the activity patterns of different subnetworks. Furthermore, our study with the DREADD approach provided compelling evidence that enhancing GABAergic inputs can augment subnetwork coherence.

Elucidating when and how neuronal subnetworks are established has been challenging, as training neonatal mice for specific tasks is impractical. The other challenge is the longitudinal imaging of developing pups started with minimal motor movements to sudden increase in physical activity after eye-opening, such as walking and grooming (*34*). To overcome this challenge, we focused on analyzing spontaneous activity patterns during quiescence state- neurons within the same subnetwork often coactivate during such spontaneous activity (*5, 8, 10-12*). By observing cortical activity during periods of quiescence, we identified three key aspects of spontaneous activity during the P11-P21 period: sparsification, desynchronization (characterized by burst activation of all neurons), and decorrelation (involving pairwise correlated activity of activity traces). These developmental changes were evident in both L2/3 and L4 layers across male and female mice (Fig. 1, Fig. 4, Fig. S2F), aligning with previous studies (*15, 17-21*). Furthermore, computational models of developing neural networks have demonstrated that blocking GABAergic transmission increases synchronous activity(*35*). Consistent with this, our results showed that enhancing GABAergic neuronal activity acutely reduces event frequency and synchrony frequency (Fig. 5C, D). These findings suggest that the maturation of GABAergic inputs plays a significant role in developmental sparsification and desynchronization.

Building on these observations, the developmental transition from highly synchronous activity patterns in early postnatal stages to a mature state, characterized by sparse but co-activated distinct neuronal subsets (known as ensembles or subnetworks), has significant functional implications. This mature state is thought to enhance the efficiency of information storage, retrieval, and processing (*5, 6*). In our study, we primarily utilized k-means clustering, an unsupervised algorithm, to identify neuronal subnetworks, which are

defined as clusters of recurrent activity patterns arising from spontaneous activity. To ensure the robustness of our clustering results and reduce the risk of random clustering effects, we also employed semi-supervised Louvain community algorithms.

During the event clustering process, we found that the k-means algorithm grouped approximately 25% of events, with about 1% of events being involved in event-multiple cluster (Fig. S7A). The relatively low number of events clustered may partly reflect the inherently sparse nature of neuronal activity, which is a common challenge in neuroscience. To further test the robustness of our clustering results, we employed additional similarity matrices, including cosine similarity and Jaccard similarity, for k-means clustering (Fig. S7B-C). Cosine similarity is particularly effective with dense data, where many attributes are present, and values are non-zero, as it considers the vector orientation. In contrast, Jaccard similarity is better suited for sparse data, where attributes are mostly absent or binary, focusing on the overlap between sets. When comparing the results obtained using these additional similarity matrices, we observed that the covariance matrix grouped the highest number of events and consequently formed more subnetworks (Figure. S7A-C). This finding indicated that the covariance matrix provided the optimal clustering performance for our data.

In addition to applying different similarity matrices, we also tested two Louvain community detection algorithms, the uniform model and the asymmetric model, using the covariance matrix. The uniform model assumes that the network is undirected and unweighted, treating all edges equally and focusing solely on the structure to detect communities (*36*). In contrast, the asymmetric model accounts for the direction and weight of edges, allowing for the separate handling of positive and negative correlations (*37*). Our results revealed that k-means clustering and Louvain community detections clustered a similar percentage of events (Fig. S7A, D-E). However, Louvain community identified fewer neuronal subnetworks compared to the k-means clustering algorithm (Fig. S7A, D-E). Importantly, all four additional clustering methods demonstrated developmental increases in silhouette values and stability in subnetwork numbers (Fig. S7). Moreover, reductions in the percentage of single-cluster neurons and increases in the percentage of non-cluster neurons were consistently observed with both Louvain community detection algorithms (Fig. S8). In conclusion, the clustering outcomes are robust and reliable, indicating that the observed decrease in the percentage of neurons participating in subnetworks is unlikely to be attributed to the sparseness of neuronal activity.

377 During our investigation, most imaged neurons (~90%) were identified as glutamatergic
378 neurons, while approximately 10% were categorized as GABAergic neurons (Fig. S5E). It
379 is plausible that both excitatory and inhibitory neurons contributed to the formation of
380 subnetworks observed in our study. Notably, neuronal subnetworks had already emerged
381 as early as P11, the first day of our imaging, although they exhibited lower coherence at
382 this stage (Fig. 2D, Fig. 4D). However, at P11, the neuronal activity patterns of different
383 subnetworks were quite similar, whereas by P21, activity patterns become more
384 individualized for each subnetwork (Fig. 2C).

385 From P11 to P21, we observed a reconfiguration of nascent subnetworks, characterized by
386 a decrease in the percentage of neurons participating in each subnetwork (Fig. 3A-C, Fig.
387 S4F-H). We propose that the transition from a larger, less-coherent set of neurons to a
388 smaller, more cohesive neuronal group is a developmental strategy to enhance the activity
389 coherence of nascent subnetworks, and subsequently stabilize their functional
390 performance. Ideally, tracking the same groups of neurons over time would provide more
391 insights, but technical challenges posed by developmental brain expansion limit our ability
392 to reliably trace more than 50 neurons, the number required for clustering analysis. Future
393 studies could benefit from incorporating cellular markers to help identify and track the
394 same neurons across longitudinal imaging studies.

395 A recent computational study on large-scale cortical network assembly demonstrated that
396 networks dominated by excitatory interactions exhibited rapid assembly formation, though
397 this often involved the recruitment of additional, non-perturbed neurons, leading to some
398 nonspecific activation (*38*). Conversely, networks with strong excitatory and inhibitory
399 interactions formed assemblies that are more confined to the perturbed neurons (*38*). In
400 line with these findings, we observed a transition in subnetwork configuration from a high
401 to lower participation rate between the 2nd to 3rd postnatal week (Fig. 4F-H), which
402 coincided with an increase in cortical inhibitory inputs (*24, 25*). Moreover, acute
403 enhancement of GABAergic activity also reduced the percentage of neurons participating
404 in subnetworks (Fig. 5F). These observations suggest that inhibitory inputs play a crucial
405 role in excluding non-perturbed neurons from staying within subnetworks.

406 Following this, an important question arises: what advantages do neurons gain from being
407 restricted to individual subnetworks during development? In the mature S1 cortex, strong
408 recurrent excitatory connectivity provides a robust framework for performing complex
409 computational tasks (*39-42*). However, networks with high excitatory gain can be prone to

410 instability. In contrast, inhibitory inputs provide a dynamic and flexible mechanism for
411 stabilizing these potentially unstable networks (*42-44*). At P11, we noted that nascent
412 event clusters exhibited the lowest silhouette values (Fig. 2D, 4D), likely reflecting an
413 early stage when excitatory intra-cortical connections were just established (*26, 27*) and
414 inhibitory inputs remained weak (*24, 25*). As development progressed, particularly by
415 P21, these event clusters showed high silhouette values, indicating either a more uniform
416 activity pattern within individual subnetworks or more distinct patterns among different
417 subnetworks. Importantly, this increase in similarity was observed when GABAergic
418 neuronal activity was acutely elevated (Fig. 4E). These findings reinforce the idea that
419 GABAergic inputs contribute significantly to enhancing the functional coherence of
420 subnetworks during development.

421 At P15, we observed that male mice exhibited larger silhouette values compared to female
422 mice in both L2/3 and L4 (Fig. 4D). However, our anatomical studies quantifying the
423 densities of overall GABAergic input in neuropil and perisomatic GABAergic input did
424 not reveal any sex-dependent differences (Fig. S9A, C-E). Our data do show differences
425 between L2/3 and L4: (1) L4 exhibited a higher density of putative parvalbumin synapses
426 labeled by Syt2 antibody (44), but not total GABAergic synapses marked by VGAT,
427 compared to L2/3 (Fig. S9D-E); (2) L4 spiny stellate neurons not only have significantly
428 smaller somatic volumes (Fig. S9F) but also receive less perisomatic GABAergic inputs
429 than L2/3 neurons (Fig. S9G). When drivers for immature GABAergic neurons become
430 available, it will be important to explore when each subtype of GABAergic neurons
431 begins to engage in perisomatic or neuropil regions in different cortical layers and how
432 they contribute to the functional maturation of neuronal subnetworks.

433 Sensorimotor developmental studies reveal that mice begin bilateral whisking at P10 and
434 actively explore their environment with their whiskers by P11(*23, 45*). Future studies
435 investigating how thalamus- and sensory experience-dependent mechanisms influence the
436 assembly of neuronal subnetworks will be needed. Optogenetic or electrical stimulation of
437 L2/3 pyramidal neurons in brain slices from the adult mouse visual cortex has been shown
438 to induce neuronal ensemble formation, which is accompanied by an increase in intrinsic
439 excitability (*46*). Reducing this heightened intrinsic excitability reverses ensemble
440 formation, highlighting its role in the process (*46*). Thus, future studies should be
441 conducted to test if increasing intrinsic excitability in developing cortical neurons can
442 facilitate the functional assembly of cortical subnetworks.

In summary, our study demonstrates early formation of subnetworks structures among S1 neurons in upper cortical layers, with a gradual increase in coherence during the 2nd to 3rd postnatal weeks. This maturation process involves retaining neurons with similar activity patterns within the subnetwork to enhance functional coherence. Furthermore, our findings highlight the role of GABAergic inputs in shaping subnetwork coherence.

449 **Materials and Methods**

450 Experimental Design

451 Most of the animals used in this study were of a C57/B6J background. To increase the
452 sample size for meaningful statistical comparisons, we also included wild-type animals
453 from genetically modified lines, which, although primarily C57/B6J, were less pure. In
454 figures 1 and 2, Some animals in figures 1 and 2 are mixed C57/B6J with R26-LSL-
455 hM4Di-DREADD or R26-LSL-Gq-DREADD or FGF9 cKO mice (NEX-Cre negative,
456 *FGF9*$^{flox/flox}$, GAD-GFP). All animals in figure 6 were C57/B6J mice. Both male and
457 female mice were used for data analysis. All procedures involving animals were
458 performed in accordance with the Indiana University Bloomington Animal Research
459 Committee, and the NIH Guide for the Care and Use of Laboratory Animals.

460

461 P1/P2 injection of AAV for jRGECO1a expression

462 The surgical procedure was conducted as described previously (*18*) with slight
463 modification. pAAV9. Syn.NES-JRGECO1a (100854-AAV9) and pAAV9.hDlx-
464 GqDREADD-dTomato (83897-AAV9) viruses were purchased from Addgene and diluted
465 to a working titer of $1x10^{13}$ GC/ml with 0.05% FastGreen FCF dye. Postnatal one- or two-
466 day pups were anesthetized with isoflurane (5% for induction, 2-3% maintenance via a
467 nose cone, vol/vol). Subcutaneous injection of ketofen (5mg/kg) was administered. The
468 surgical region was disinfected with 4% chlorhexidine and 70% alcohol. We used soft
469 silicone ear bars to position the mouse on the stereotaxic frame to make the desired
470 injection area (presumptive somatosensory cortex) as flat as possible. We used scissors to
471 create a 3-4 mm triangular skin flap over S1. The periosteum was gently cleared under the
472 skin flap using a sterile cotton swab. The skin flap (folded back) was covered with a piece
473 of saline-soaked Gelfoam to prevent the skin from drying during the procedure. At the
474 injection site, the bone was drilled lightly to create a small crack, permitting injection via
475 pulled-glass capillary without exposing the dura. Glass micropipettes (O.D. 1 mm, I.D. 0.5
476 mm Sutter Instruments, cat no. BF100-50-10) pulled by using a P1000 pipette puller
477 (Shutter Instruments, CA, USA) were used to inject ~200 nL of AAV into the superficial
478 cortex, using an injection pump equipped with a Hamilton syringe. The pipettes were
479 positioned for injection at 70~90° angle to the skull surface and gently pierced through the
480 cracked bone and into the superficial cortex. The injection flow rate was 50 nL/min. The

481 light blue dye was visible on the brain surface of pups with successful injection. The glass
482 pipettes were left in place for one minute before withdrawal. The skin flap was sealed with
483 a small drop of VetBond to the injection site. The entire surgery was complete in 10-15
484 min per pup. The pups recovered on a warm blanket before being returned to the dam.

485

486 Cranial window surgery

487 The surgical procedure was conducted as previously described (*18*) with slight
488 modification. Mice aged at P8~ 9 were anesthetized with 5% isoflurane for induction,
489 followed by 2-3% maintenance (vol/vol, via nose cone). Pups also received Ketoprofen (5
490 mg/kg, s.c.), Dexamethasone (1 mg/kg, s.c.), and a mixture of lidocaine and epinephrine
491 (4 mg/kg and 0.1 mg/kg, respectively, applied topical to the surgical region) for analgesia
492 and anti-inflammatory purposes. Pups were positioned using blunt ear bars on the
493 stereotaxic frame. The original AAV injection site was visible as a well-healed triangular
494 scar on the skin. The pup's head was swabbed with 4% chlorhexidine and 70% alcohol to
495 disinfect the skin and the skin over the surgical area was removed. A dental drill was used
496 to carve a circular craniotomy, 3 mm in diameter. The drilling was stopped once the bone
497 had cracked around the perimeter of the craniotomy. Any blood was promptly cleared to
498 prevent a blurred window. The entire drilled area was soaked with sterile saline using
499 Gelfoam for at least 3 min to soften the bone. The bone fragment was gently removed, and
500 a 3 mm glass plug coverslip (generated by adhering 2.3 mm coverslip with optical
501 transparent UV-activated adhesive) was positioned over the craniotomy. The glass was
502 sealed using cyanoacrylate then dental acrylic (Metabond). A custom-made circular head
503 plate (less than 0.5 g, Fig. S1C) was positioned over the area, centered around the cranial
504 window, and was adhered to the skull using dental acrylic (Metabond). The pup was then
505 placed on a heating pad with bedding for recovery and then returned to the dam when
506 fully mobile. Post-surgical pups were fed with kitten milk replacement (every 4-5 hours
507 during daytime) to provide nutrition if pups did not gain body weight and had no milk spot
508 in the belly. Pups became more active in seeking the dam for milk two days after the
509 surgical procedure. Pups were subjected to habituation on the imaging station for 15
510 minutes the day after surgery. Following that, pups were habituated on the imaging station
511 for 30 minutes (the average imaging time) or subjected to the imaging procedure daily.
512 During our imaging period, pups continued to gain body weight as they grew up (Fig.
513 S1E).

514

515 *In vivo* calcium imaging in head-restrained neonatal pup

516 Before imaging, a metal bar was attached to the headframe to provide the anchoring point
517 to the imaging station (Fig. S1B, C). Calcium imaging was performed on a Nikon A1R
518 MP^+ two photon microscope, with an Insight DeepSee pulsed laser (Spectra-Physics Inc,
519 Santa Clara, USA), resonant scanner, a 25x, 1.1 NA water immersion lens (Nikon, Japan),
520 and Nikon Elements software. The homemade imaging station was equipped with a
521 lightweight foam disc covered by a circular paper drape. The center of the disc was fixed,
522 allowing pups to rest, whisk, or walk with minimal friction (Fig. S1D). A heating pad was
523 placed under the imaging platform to maintain the body temperature of neonatal pups. The
524 light source was an Insight laser at 1040 nm for jRGECO1a. Whole field images were
525 acquired at 65.6 ms/frame (~15.23 Hz) with a resolution of 512 x 512 pixels. The pups'
526 body movements were simultaneously monitored and recorded during the imaging
527 procedure using infrared cameras (Fig. S1D). USB cameras (30 Hz) with an 850 nm IR
528 LED light source and IR-cut filter at 850 nm were used to record body movements. A
529 Flea3 USB3 camera (100 Hz) with an IR-cut filter at 850 nm was used to record whisker
530 movements. Before calcium imaging, pups were habituated on the imaging station for at
531 least 10 mins. To find the same field of view to image in subsequent imaging sessions, we
532 used the vasculature pattern as a landmark to locate the previous imaging position (Fig.
533 S1F). First, the global vasculature pattern in the cranial window was imaged by using a
534 dissecting microscope (Fig. S1F upper panel). The location where calcium imaging was
535 performed was marked on the map. Next, the pial surface vasculature pattern was imaged
536 under the two-photon microscope and used as a second landmark (Fig. S1F lower panel).
537 Each imaging session was conducted within one hour per animal to minimize the adverse
538 effects of maternal separation. For imaging in L2/3, the location was set at 120-150 μm
539 below the pia surface. while for L4, it was adjusted to 200-350 μm below the pia surface.
540 After the final imaging session, some pups were perfused to confirm the imaged area was
541 in S1 (Fig. S1G).

542

543 Data analysis for calcium imaging

544 The preprocessing of all raw calcium movie data was done using a Suites2P toolbox (*47,*
545 *48*). Briefly, Suite2p first aligned all frames of a calcium movie using two-dimensional

546 rigid registration based on regularized phase correlation, subpixel interpolation, and
547 kriging. Suite2p computed a low-dimensional decomposition of the data using a clustering
548 algorithm that finds regions of interest (ROIs) based on the correlation of the pixels inside
549 them. We inspected every ROI using the following criteria: (1) the classical morphology
550 should be a donut-shaped circle because the cytosolic distributions of jRGECO1a; (2) the
551 neurons with obvious nuclear signals were excluded, as were cells from animals injected
552 with pAAV9-hDlx-GqDREADD-dTomato expressed nuclear dTomato fluorescent protein
553 (fig. S6); (3) ROIs never overlapped. For the neuropil correction, we used the Fast
554 Imaging Signal Separation Analysis (FISSA) toolbox (*49*). The coordinates of selected
555 ROIs and post-motion-corrected tiff files were imported to the FISSA toolbox for neuropil
556 decontamination. After neuropil correction, the $\Delta F/F$ was calculated as $(F-F_0)/F_0$. Where
557 the F is the extracted fluorescence signal, and F_0 is the median of the bottom 10th
558 percentile of the fluorescent trace. To normalize the differential fluorescent change caused
559 by the expressed jRGECO1a level in each neuron, we further calculated the modified Z
560 score for each neuron (*50, 51*). Zscore = F(t) - mean(baseline) / std (baseline). Where the
561 baseline period is the 10-s period with the lowest variation (s.t.d.) in $\Delta F/F$. We used the
562 Peakfinder function in MatLab to find the conceivable calcium transient referred to
563 neuronal spike activity (Fig. S1D). The detected calcium event is defined as the
564 fluorescent peak amplitude greater than four times the noise level. The noise level is the
565 mean Z score within five second-time windows when it has the lowest root mean square
566 (Fig. S1D). To analyze the spontaneous neuronal activity, we used the DeepLabCut
567 toolbox (*52, 53*) to annotate the movement of the limbs and identify the time windows
568 when pups show minimum activity (stationary condition). In addition, the video-recorded
569 facial movements were analyzed by Facemap Python package (*48*). Both annotations were
570 plotted to visualize the overall movement of the body and whisker (Fig. S1E). For
571 spontaneous activity quantification, the time period with minimum body movement and
572 whisking was used for calculating various parameters (Fig. S1E).

573 The synchrony frequency analysis was performed as described previously (*20*). We
574 reconstructed activity histograms that plotted the percent of active cells for each frame
575 (Fig. 1E). The threshold for detecting a network event was set by repeatedly shuffling
576 each deconvolved somatic calcium trace 100 times while maintaining the average firing
577 rate for each cell. A surrogate activity histogram was constructed from each reshuffled
578 trial. The threshold was calculated by first finding the peak percentage of cells active in

each reshuffled trial, and then sorting these values to find the 95th percentile, which was set as the threshold for significance (p=0.05). The time point when the percent of active neurons exceeded this threshold was set as the start of an event. The time point when the percentage of active neurons fell below this level was set as the end of the event. The mean frequency of peaks of synchrony and the mean fraction of active cells at the maximum point of each peak of synchrony were calculated. For the pairwise correlation analysis, we computed the Pearson correlation coefficient for Z-score normalized traces during stationary status.

To identify the neuronal subnetwork, we employed a similar strategy as previously described (*11, 16*). The initial calcium event clusters were identified using a clustering algorithm based on calcium dynamic similarity. Unsupervised clustering of calcium events was obtained by using the k-means algorithm on the normalized covariance matrix (frame-frame) with cluster numbers ranging from 2-19. One hundred iterations of k-means were run for each cluster number, and the iteration that resulted in the best-average silhouette value was retained. Each cluster was then associated to a cell assembly that comprised those neurons that significantly participated in the events within that particular cluster. Cell participation in a given cluster was considered statistically significant if the fraction of synchronous events in that cluster that activated the cell exceeded the 95th percentile of reshuffled data. If a neuron was significantly active in more than one cluster, it was associated with the one in which it participated the most (based on percentage). The overlap between assemblies/subnetworks was quantified by calculating the silhouette value of each cell (with the normalized hamming distance between each cell pair as a dissimilarity metric). A neuron was significantly involved in a single cluster if its silhouette value was higher than expected by chance (95th percentile after reshuffling). Events were finally sorted with respect to their projection onto neuronal subnetworks (Fig. S3A-B). Alternatively, neurons were grouped according to their subnetwork identities (Fig. 2C). We computed the tCC for detected event (binary format) for all possible neuronal pairs or neuronal pairs within their subnetwork or between subnetwork.

To test the robustness of the k-means clustering results, we compared our results to those obtained from two alternative similarity metrices: cosine similarity and Jaccard similarity. We replaced the covariance matrix with the respective alternate values and completed the remaining steps of analyses identically. In addition to unsupervised k-means clustering algorithm, we also utilized semi-supervised Louvain community detection algorithm (*54-*

612 *56*) to cluster the calcium event. Two commonly used models, the uniform null model (*36*)
613 and the asymmetric model (*37*), both developed for the neuroscience field, were chosen to
614 cluster the covariance similarity matrix. Five hundred and 100 iterations were run for the
615 uniform and asymmetric models followed by 10 iterations of consensus clustering without
616 removing any weak elements (*57*). The iteration numbers were chosen based on clustering
617 result reach converge. After the community detection algorithm identified the event
618 cluster, we completed the remaining steps of analyses identically to cluster the calcium
619 event. After the community detection algorithm identified the event cluster, we completed
620 the remaining steps of analyses identically.

621

622 Immunohistochemistry, imaging, and quantification

623 Mice were deeply anesthetized with isoflurane and subsequently perfused with 4%
624 paraformaldehyde in phosphate-buffered saline (PBS) at a rate of approximately 2
625 mL/minute for a duration of ten minutes. Fixed brains were then sectioned into 100 μm
626 sections in the coronal plane using a Leica VT-1000 vibrating microtome (Leica
627 Microsystems) and stored in an antigen-preserved solution (consisting of PBS, 50%
628 ethylene glycol, and 1% polyvinyl pyrrolidone) at -20 °C until further analysis. Sections
629 were permeabilization with 2% Triton X-100 and then incubated in a blocking solution
630 (3% normal goat serum in PBS with 0.3% Triton X-100). Primary antibodies, prepared in
631 the blocking solution, were applied overnight. Detection of primary antibodies was
632 achieved using the appropriate secondary antibody conjugated with an Alexa series
633 fluorophore was utilized. DAPI (100 ng/ml, ThermoFisher) was included in the secondary
634 antibody solution to stain nuclei. For cell counting, Z-stack confocal images were captured
635 from both hemispheres using a Nikon A1 confocal microscope equipped with a
636 10X/NA0.45 objective. Z-stacks were acquired at 1 μm intervals, resulting in a total
637 imaged thickness of 5 μm. Quantification of colocalization between different markers,
638 was performed using single-plane images, and analysis was carried out with NIH ImageJ
639 software.

640 For the quantification of inhibitory synapses, Z-stack confocal images were obtained using
641 a Nikon A1 confocal microscope with a 60X/NA1.4 objective at three times software
642 zoom. The Z-stack was captured at 0.1 μm intervals, and each Z-stack contained 1 to 3
643 somas per image. Two images from each hemisphere were captured for each animal, and

644 images from both hemispheres were analyzed using Imaris software (Bitplane, Zurich,
645 Switzerland) following a workflow based on previous published methodologies (*58-63*).
646 Given the variability in the volume occupied by nuclei and vasculature in each image,
647 which influenced synaptic marker density quantification, surface objects of nuclei and
648 vasculature-like structures were created using the Imaris surface module. The VGAT- or
649 Syt2-channel was masked by these objects to exclude the volume they occupied. The post-
650 masked VGAT channel was used to generate a surface object (referred to as the neuropil
651 object) for analysis. To analyze VGAT and Syt2 double-positive puncta, the ImarisColoc
652 function was employed to generate a new channel containing the VGAT and Syt2
653 colocalized signal, which was then used for subsequent spot detection. For spot detection,
654 synaptic puncta labeled with VGAT, Syt2, and VGAT/Syt2 colocalized puncta were
655 detected using the Imaris spot module with a diameter threshold of 0.5 µm. Synaptic
656 puncta typically range in diameter ranging from 0.25–0.8 (*64, 65*). To determine the
657 optimal detection threshold, the threshold was manually defined for one image from each
658 animal, and the threshold that detected the most synaptic puncta without creating artifacts
659 was applied to analyze all images. This generated a spot layer for each synaptic marker
660 channel. Synaptic density was calculated as the number of detected synapses inside the
661 neuropil object divided by the neuropil volume. For peri-somatic inhibitory synapse
662 quantification, the surface objects were created based on Kv2.1 signal using the surface
663 module. VGAT, Syt2, and VGAT/Syt2 double-positive puncta located within 0.25 µm of
664 the soma object were defined as perisomatic inhibitory synapses. All image acquisition
665 and data analysis procedures were conducted in a blinded manner.

666

667 <u>Statistical analysis</u>

668 Given the clustered nature of the experimental design (*28-30*), we primarily employed
669 linear mixed-effects (LME) models for multilevel statistical analysis to determine the
670 statistical significance for all data. In cases where the data did not exhibit clustering, we
671 fitted linear regression (LM) models instead to assess the statistical significance. We
672 further refined the models by removing interaction terms that did not improve model fits
673 based on measures such as Aikake Information Criterion and Bayesian Information
674 Criterion values. To obtain reliable and unbiased estimates of variance components in both
675 LME and LM analyses, we employed a bootstrapping procedure to resample the dataset
676 (n=10,000) to create simulated samples (*28, 29*). With this information, we conducted

post-hoc comparisons using the bootstrapping output as the final statistical results. Each data point or line depicted in the figures represents an individual dataset. Errors reported in the figures are presented as mean ± 95% confidence intervals of the bootstrapping output, unless otherwise indicated. Original data values and detailed statistical comparisons for all figures are provided in the extended data. Given that data values are not normally distributed, we employed Spearman correlation coefficient to assess the correlation between subnetwork number and neuronal number or time intervals.

686 **References**

687 1. W. C. Lee, V. Bonin, M. Reed, B. J. Graham, G. Hood, K. Glattfelder, R. C. Reid,
688 Anatomy and function of an excitatory network in the visual cortex. *Nature* **532**, 370-374
689 (2016).
690 2. L. Cossell, M. F. Iacaruso, D. R. Muir, R. Houlton, E. N. Sader, H. Ko, S. B. Hofer, T. D.
691 Mrsic-Flogel, Functional organization of excitatory synaptic strength in primary visual
692 cortex. *Nature* **518**, 399-403 (2015).
693 3. Y. Yoshimura, J. L. Dantzker, E. M. Callaway, Excitatory cortical neurons form fine-scale
694 functional networks. *Nature* **433**, 868-873 (2005).
695 4. S. P. Peron, J. Freeman, V. Iyer, C. Guo, K. Svoboda, A Cellular Resolution Map of
696 Barrel Cortex Activity during Tactile Behavior. *Neuron* **86**, 783-799 (2015).
697 5. K. D. Harris, T. D. Mrsic-Flogel, Cortical connectivity and sensory coding. *Nature* **503**,
698 51-58 (2013).
699 6. L. Yassin, B. L. Benedetti, J. S. Jouhanneau, J. A. Wen, J. F. Poulet, A. L. Barth, An
700 embedded subnetwork of highly active neurons in the neocortex. *Neuron* **68**, 1043-1050
701 (2010).
702 7. M. Agetsuma, J. P. Hamm, K. Tao, S. Fujisawa, R. Yuste, Parvalbumin-Positive
703 Interneurons Regulate Neuronal Ensembles in Visual Cortex. *Cereb Cortex* **28**, 1831-1845
704 (2018).
705 8. J. E. Miller, I. Ayzenshtat, L. Carrillo-Reid, R. Yuste, Visual stimuli recruit intrinsically
706 generated cortical ensembles. *Proc Natl Acad Sci U S A* **111**, E4053-4061 (2014).
707 9. R. Yuste, R. Cossart, E. Yaksi, Neuronal ensembles: Building blocks of neural circuits.
708 *Neuron* **112**, 875-892 (2024).
709 10. S. Peron, R. Pancholi, B. Voelcker, J. D. Wittenbach, H. F. Olafsdottir, J. Freeman, K.
710 Svoboda, Recurrent interactions in local cortical circuits. *Nature* **579**, 256-259 (2020).
711 11. A. Malvache, S. Reichinnek, V. Villette, C. Haimerl, R. Cossart, Awake hippocampal
712 reactivations project onto orthogonal neuronal assemblies. *Science* **353**, 1280-1283
713 (2016).
714 12. L. Carrillo-Reid, W. Yang, Y. Bando, D. S. Peterka, R. Yuste, Imprinting and recalling
715 cortical ensembles. *Science* **353**, 691-694 (2016).
716 13. N. Anton-Bolanos, A. Sempere-Ferrandez, T. Guillamon-Vivancos, F. J. Martini, L.
717 Perez-Saiz, H. Gezelius, A. Filipchuk, M. Valdeolmillos, G. Lopez-Bendito, Prenatal
718 activity from thalamic neurons governs the emergence of functional cortical maps in mice.
719 *Science* **364**, 987-990 (2019).
720 14. V. Moreno-Juan, A. Filipchuk, N. Anton-Bolanos, C. Mezzera, H. Gezelius, B. Andres, L.
721 Rodriguez-Malmierca, R. Susin, O. Schaad, T. Iwasato, R. Schule, M. Rutlin, S. Nelson,
722 S. Ducret, M. Valdeolmillos, F. M. Rijli, G. Lopez-Bendito, Prenatal thalamic waves
723 regulate cortical area size prior to sensory processing. *Nat Commun* **8**, 14172 (2017).
724 15. H. Mizuno, K. Ikezoe, S. Nakazawa, T. Sato, K. Kitamura, T. Iwasato, Patchwork-Type
725 Spontaneous Activity in Neonatal Barrel Cortex Layer 4 Transmitted via Thalamocortical
726 Projections. *Cell Rep* **22**, 123-135 (2018).
727 16. L. Modol, Y. Bollmann, T. Tressard, A. Baude, A. Che, Z. R. S. Duan, R. Babij, N. V. De
728 Marco Garcia, R. Cossart, Assemblies of Perisomatic GABAergic Neurons in the
729 Developing Barrel Cortex. *Neuron* **105**, 93-105 e104 (2020).
730 17. S. Nakazawa, Y. Yoshimura, M. Takagi, H. Mizuno, T. Iwasato, Developmental Phase
731 Transitions in Spatial Organization of Spontaneous Activity in Postnatal Barrel Cortex
732 Layer 4. *J Neurosci* **40**, 7637-7650 (2020).

18. C. X. He, E. D. Arroyo, D. A. Cantu, A. Goel, C. Portera-Cailliau, A Versatile Method for Viral Transfection of Calcium Indicators in the Neonatal Mouse Brain. *Front Neural Circuits* **12**, 56 (2018).
19. P. Golshani, J. T. Goncalves, S. Khoshkhoo, R. Mostany, S. Smirnakis, C. Portera-Cailliau, Internally mediated developmental desynchronization of neocortical network activity. *J Neurosci* **29**, 10890-10899 (2009).
20. J. T. Goncalves, J. E. Anstey, P. Golshani, C. Portera-Cailliau, Circuit level defects in the developing neocortex of Fragile X mice. *Nat Neurosci* **16**, 903-909 (2013).
21. R. Babij, C. Ferrer, A. Donatelle, S. Wacks, A. M. Buch, J. E. Niemeyer, H. Ma, Z. R. S. Duan, R. N. Fetcho, A. Che, T. Otsuka, T. H. Schwartz, B. S. Huang, C. Liston, N. V. De Marco Garcia, Gabrb3 is required for the functional integration of pyramidal neuron subtypes in the somatosensory cortex. *Neuron* **111**, 256-274 e210 (2023).
22. Y. Bollmann, L. Modol, T. Tressard, A. Vorobyev, R. Dard, S. Brustlein, R. Sims, I. Bendifallah, E. Leprince, V. de Sars, E. Ronzitti, A. Baude, H. Adesnik, M. A. Picardo, J. C. Platel, V. Emiliani, D. Angulo-Garcia, R. Cossart, Prominent in vivo influence of single interneurons in the developing barrel cortex. *Nat Neurosci* **26**, 1555-1565 (2023).
23. A. van der Bourg, J. W. Yang, V. Reyes-Puerta, B. Laurenczy, M. Wieckhorst, M. C. Stuttgen, H. J. Luhmann, F. Helmchen, Layer-Specific Refinement of Sensory Coding in Developing Mouse Barrel Cortex. *Cereb Cortex* **27**, 4835-4850 (2017).
24. A. Gour, K. M. Boergens, N. Heike, Y. Hua, P. Laserstein, K. Song, M. Helmstaedter, Postnatal connectomic development of inhibition in mouse barrel cortex. *Science* **371**, (2021).
25. K. Kalemaki, A. Velli, O. Christodoulou, M. Denaxa, D. Karagogeos, K. Sidiropoulou, The developmental changes in intrinsic and synaptic properties of prefrontal neurons enhance local network activity from the second to the third postnatal weeks in mice. *Cereb Cortex* **32**, 3633-3650 (2022).
26. M. C. Ashby, J. T. Isaac, Maturation of a recurrent excitatory neocortical circuit by experience-dependent unsilencing of newly formed dendritic spines. *Neuron* **70**, 510-521 (2011).
27. F. Valiullina, D. Akhmetshina, A. Nasretdinov, M. Mukhtarov, G. Valeeva, R. Khazipov, A. Rozov, Developmental Changes in Electrophysiological Properties and a Transition from Electrical to Chemical Coupling between Excitatory Layer 4 Neurons in the Rat Barrel Cortex. *Front Neural Circuits* **10**, 1 (2016).
28. S. Galbraith, J. A. Daniel, B. Vissel, A study of clustered data and approaches to its analysis. *J Neurosci* **30**, 10601-10608 (2010).
29. E. Aarts, M. Verhage, J. V. Veenvliet, C. V. Dolan, S. van der Sluis, A solution to dependency: using multilevel analysis to accommodate nested data. *Nat Neurosci* **17**, 491-496 (2014).
30. M. B. de Melo, D. Daldegan-Bueno, M. G. Menezes Oliveira, A. L. de Souza, Beyond ANOVA and MANOVA for repeated measures: Advantages of generalized estimated equations and generalized linear mixed models and its use in neuroscience research. *Eur J Neurosci* **56**, 6089-6098 (2022).
31. Z. Yu, M. Guindani, S. F. Grieco, L. Chen, T. C. Holmes, X. Xu, Beyond t test and ANOVA: applications of mixed-effects models for more rigorous statistical analysis in neuroscience research. *Neuron* **110**, 21-35 (2022).
32. J. D. Dorn, D. L. Ringach, Estimating membrane voltage correlations from extracellular spike trains. *J Neurophysiol* **89**, 2271-2278 (2003).
33. J. Dimidschstein, Q. Chen, R. Tremblay, S. L. Rogers, G. A. Saldi, L. Guo, Q. Xu, R. Liu, C. Lu, J. Chu, J. S. Grimley, A. R. Krostag, A. Kaykas, M. C. Avery, M. S. Rashid, M. Baek, A. L. Jacob, G. B. Smith, D. E. Wilson, G. Kosche, I. Kruglikov, T. Rusielewicz, V.

C. Kotak, T. M. Mowery, S. A. Anderson, E. M. Callaway, J. S. Dasen, D. Fitzpatrick, V. Fossati, M. A. Long, S. Noggle, J. H. Reynolds, D. H. Sanes, B. Rudy, G. Feng, G. Fishell, A viral strategy for targeting and manipulating interneurons across vertebrate species. *Nat Neurosci* **19**, 1743-1749 (2016).

34. , (!!! INVALID CITATION !!! (23, 33)).

35. V. Rahmati, K. Kirmse, K. Holthoff, L. Schwabe, S. J. Kiebel, Developmental Emergence of Sparse Coding: A Dynamic Systems Approach. *Sci Rep* **7**, 13015 (2017).

36. M. Bazzi, M. A. Porter, S. Williams, M. McDonald, D. J. Fenn, S. D. Howison, Community Detection in Temporal Multilayer Networks, with an Application to Correlation Networks. *Multiscale Modeling & Simulation* **14**, 1-41 (2016).

37. M. Rubinov, O. Sporns, Weight-conserving characterization of complex functional brain networks. *Neuroimage* **56**, 2068-2079 (2011).

38. S. Sadeh, C. Clopath, Excitatory-inhibitory balance modulates the formation and dynamics of neuronal assemblies in cortical networks. *Sci Adv* **7**, eabg8411 (2021).

39. A. D. Lien, M. Scanziani, Tuned thalamic excitation is amplified by visual cortical circuits. *Nat Neurosci* **16**, 1315-1323 (2013).

40. Y. T. Li, L. A. Ibrahim, B. H. Liu, L. I. Zhang, H. W. Tao, Linear transformation of thalamocortical input by intracortical excitation. *Nat Neurosci* **16**, 1324-1330 (2013).

41. L. Y. Li, Y. T. Li, M. Zhou, H. W. Tao, L. I. Zhang, Intracortical multiplication of thalamocortical signals in mouse auditory cortex. *Nat Neurosci* **16**, 1179-1181 (2013).

42. S. Sadeh, C. Clopath, Inhibitory stabilization and cortical computation. *Nat Rev Neurosci*, (2020).

43. S. J. Cruikshank, T. J. Lewis, B. W. Connors, Synaptic basis for intense thalamocortical activation of feedforward inhibitory cells in neocortex. *Nat Neurosci* **10**, 462-468 (2007).

44. F. Pouille, A. Marin-Burgin, H. Adesnik, B. V. Atallah, M. Scanziani, Input normalization by global feedforward inhibition expands cortical dynamic range. *Nat Neurosci* **12**, 1577-1585 (2009).

45. H. Arakawa, R. S. Erzurumlu, Role of whiskers in sensorimotor development of C57BL/6 mice. *Behav Brain Res* **287**, 146-155 (2015).

46. T. Alejandre-García, S. Kim, J. Pérez-Ortega, R. Yuste, Intrinsic excitability mechanisms of neuronal ensemble formation. *eLife* **11**, e77470 (2022).

47. M. Pachitariu, C. Stringer, M. Dipoppa, S. Schröder, L. F. Rossi, H. Dalgleish, M. Carandini, K. D. Harris, Suite2p: beyond 10,000 neurons with standard two-photon microscopy. *BioRxiv*, (2017).

48. C. Stringer, M. Pachitariu, N. Steinmetz, C. B. Reddy, M. Carandini, K. D. Harris, Spontaneous behaviors drive multidimensional, brainwide activity. *Science* **364**, 255 (2019).

49. S. W. Keemink, S. C. Lowe, J. M. P. Pakan, E. Dylda, M. C. W. van Rossum, N. L. Rochefort, FISSA: A neuropil decontamination toolbox for calcium imaging signals. *Sci Rep* **8**, 3493 (2018).

50. A. Goel, D. A. Cantu, J. Guilfoyle, G. R. Chaudhari, A. Newadkar, B. Todisco, D. de Alba, N. Kourdougli, L. M. Schmitt, E. Pedapati, C. A. Erickson, C. Portera-Cailliau, Impaired perceptual learning in a mouse model of Fragile X syndrome is mediated by parvalbumin neuron dysfunction and is reversible. *Nat Neurosci* **21**, 1404-1411 (2018).

51. C. X. He, D. A. Cantu, S. S. Mantri, W. A. Zeiger, A. Goel, C. Portera-Cailliau, Tactile Defensiveness and Impaired Adaptation of Neuronal Activity in the Fmr1 Knock-Out Mouse Model of Autism. *J Neurosci* **37**, 6475-6487 (2017).

52. T. Nath, A. Mathis, A. C. Chen, A. Patel, M. Bethge, M. W. Mathis, Using DeepLabCut for 3D markerless pose estimation across species and behaviors. *Nat Protoc* **14**, 2152-2176 (2019).

833 53. A. Mathis, P. Mamidanna, K. M. Cury, T. Abe, V. N. Murthy, M. W. Mathis, M. Bethge,
834 DeepLabCut: markerless pose estimation of user-defined body parts with deep learning.
835 *Nat Neurosci* **21**, 1281-1289 (2018).
836 54. P. Baum, M. A. Vogt, P. Gass, K. Unsicker, O. von Bohlen und Halbach, FGF-2
837 deficiency causes dysregulation of Arhgef6 and downstream targets in the cerebral cortex
838 accompanied by altered neurite outgrowth and dendritic spine morphology. *Int J Dev*
839 *Neurosci* **50**, 55-64 (2016).
840 55. R. F. Betzel, K. C. Wood, C. Angeloni, M. Neimark Geffen, D. S. Bassett, Stability of
841 spontaneous, correlated activity in mouse auditory cortex. *PLoS Comput Biol* **15**,
842 e1007360 (2019).
843 56. M. Rubinov, O. Sporns, Complex network measures of brain connectivity: uses and
844 interpretations. *Neuroimage* **52**, 1059-1069 (2010).
845 57. A. Lancichinetti, S. Fortunato, Consensus clustering in complex networks. *Sci Rep* **2**, 336
846 (2012).
847 58. D. L. Haggerty, G. G. Grecco, J. Y. Huang, E. H. Doud, A. L. Mosley, H. C. Lu, B. K.
848 Atwood, Prenatal methadone exposure selectively alters protein expression in primary
849 motor cortex: Implications for synaptic function. *Front Pharmacol* **14**, 1124108 (2023).
850 59. G. G. Grecco, J. Y. Huang, B. Munoz, E. H. Doud, C. D. Hines, Y. Gao, B. Rodriguez, A.
851 L. Mosley, H. C. Lu, B. K. Atwood, Sex-Dependent Synaptic Remodeling of the
852 Somatosensory Cortex in Mice With Prenatal Methadone Exposure. *Adv Drug Alcohol*
853 *Res* **2**, (2022).
854 60. B. Zhou, L. Chen, P. Liao, L. Huang, Z. Chen, D. Liao, L. Yang, J. Wang, G. Yu, L.
855 Wang, J. Zhang, Y. Zuo, J. Liu, R. Jiang, Astroglial dysfunctions drive aberrant
856 synaptogenesis and social behavioral deficits in mice with neonatal exposure to lengthy
857 general anesthesia. *PLoS Biol* **17**, e3000086 (2019).
858 61. A. K. Simhal, Y. Zuo, M. M. Perez, D. V. Madison, G. Sapiro, K. D. Micheva,
859 Multifaceted Changes in Synaptic Composition and Astrocytic Involvement in a Mouse
860 Model of Fragile X Syndrome. *Sci Rep* **9**, 13855 (2019).
861 62. D. A. Kuljis, E. Park, C. A. Telmer, J. Lee, D. S. Ackerman, M. P. Bruchez, A. L. Barth,
862 Fluorescence-Based Quantitative Synapse Analysis for Cell Type-Specific Connectomics.
863 *eNeuro* **6**, (2019).
864 63. M. J. Fogarty, L. A. Hammond, R. Kanjhan, M. C. Bellingham, P. G. Noakes, A method
865 for the three-dimensional reconstruction of Neurobiotin-filled neurons and the location of
866 their synaptic inputs. *Front Neural Circuits* **7**, 153 (2013).
867 64. D. Dumitriu, S. I. Berger, C. Hamo, Y. Hara, M. Bailey, A. Hamo, Y. S. Grossman, W. G.
868 Janssen, J. H. Morrison, Vamping: stereology-based automated quantification of
869 fluorescent puncta size and density. *J Neurosci Methods* **209**, 97-105 (2012).
870 65. E. Kim, M. Sheng, The postsynaptic density. *Curr Biol* **19**, R723-724 (2009).
871

872

Acknowledgments

We thank Bruna Baumgarten Krebs, Joseph Kimmel Leffel, and Sarah Van Meter for their technical support. We thank Drs. Carlos Portea-Cailliau, Duton Oyesanmi, Ju Lu, Nathalie L. Rochefort, Ruth Eberle, and Sander W. Keemink for the coding support. We thank clinical veterinarian Randalyn Shepherd for excellent support and suggestions to keep post-surgical pups healthy. We thank Drs. Ehren Lee Newman, Richard Betzel, and Zoran Tiganj for the critical suggestions related to additional clustering analysis. We thank Eric Wernert, Esen Tuna, and James Robert McCombs for assisting with data storage and using high-performance computing resources. We thank Miss Pei-Ying Chen from the Indiana Statistical Consulting Center for assisting with statistical analysis. We also thank Drs. Cary Lai, Ehren Lee Newman, Ken Mackie, Richard Betzel, Wei-Hsiang Huang, and Zoran Tiganj for their helpful comments.

Funding:

National Institutes of Health grant R01NS086794 (HCL)

National Institutes of Health grant P30DA056410 (HCL)

startup funds from the IUB College of Arts and Sciences (HCL)

Gill endowment funds (HCL)

Indiana Clinical and Translational Sciences Institute funded, in part by Grant Number UL1TR002529 from the National Institutes of Health National Center for Advancing Translational Sciences, Clinical and Translational Sciences Award. The content is solely the responsibility of the authors and does not necessarily represent the official views of the National Institutes of Health

Lilly Endowment, Inc., through its support for the Indiana University Pervasive Technology Institute

Shared University Research grants from IBM, Inc., to Indiana University. This work used the Extreme Science and Engineering Discovery Environment (XSEDE), which is supported by National Science Foundation grant number ACI-1663578

Author contributions:

Conceptualization: JYH, HCL

Methodology: JYH, MH, AB, SJB

Investigation: JYH, LNH, XL, AJX

Visualization: JYH, MH, SJB, XL

Supervision: JYH, HCL

Writing—original draft: JYH, MH, HCL

Writing—review & editing: JYH, MH, AB, XL, LNH, AJX, SJB, HCL

Competing interests:

The authors declare no competing interests.

Data and materials availability:

All raw data reported in this paper were uploaded to DataJoint company (https://www.datajoint.com/) and will be shared by the lead contact upon request. All codes for data analysis and statistical comparison test and post-analyzed files can be found at https://github.com/EdnaHuang/SubnetworkAssembley2024". Codes and data are also available from the Jui-Yen Huang upon request. Additionally, the data analysis workflow is incorporated into elements of DataJoint for public use.

Figures and Tables

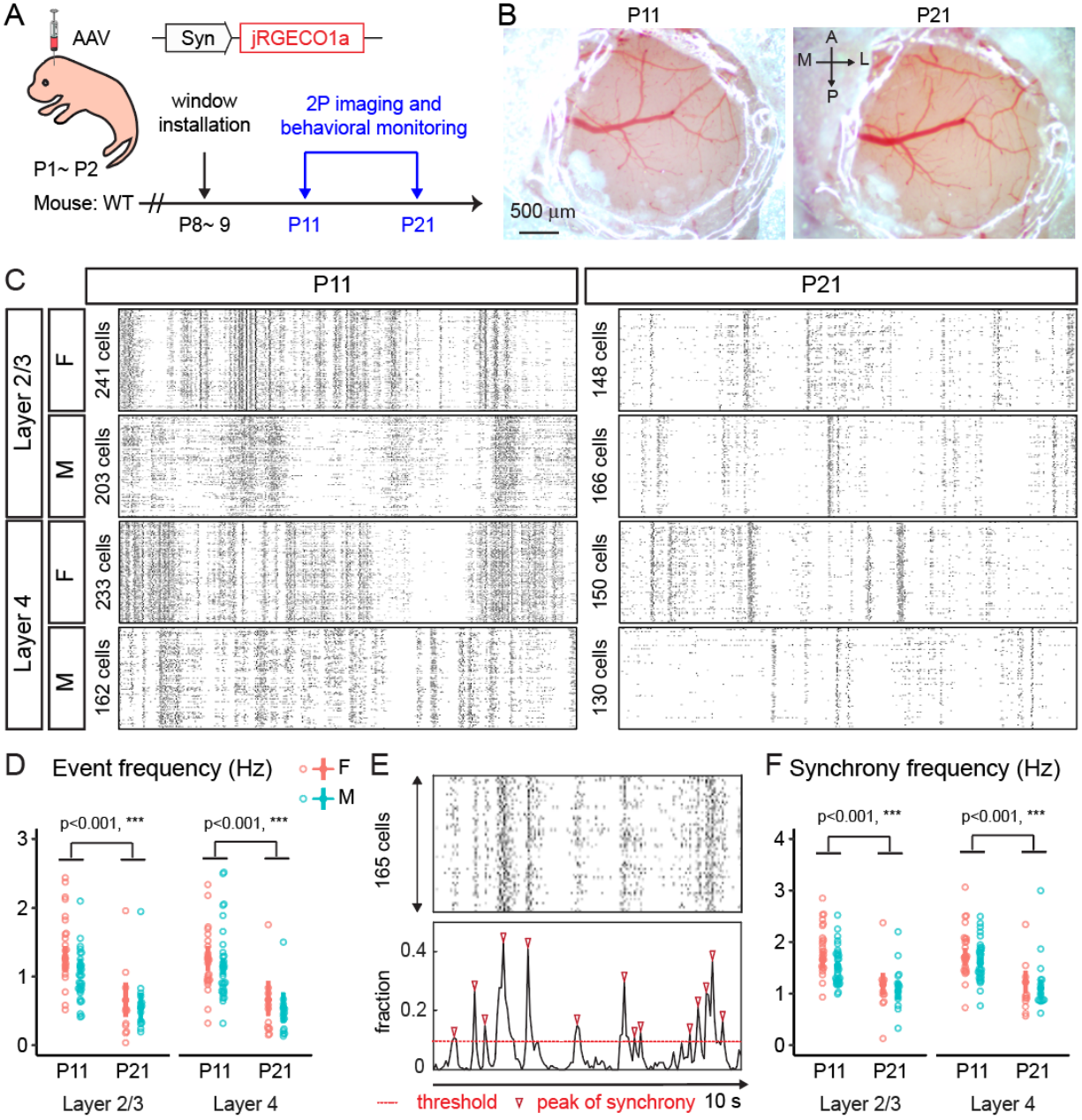

Fig. 1. Spontaneous neuronal activity gradually decreased and desynchronized in both L2/3 and L4, irrespective of sex, with increasing age.

(A) Schematic of the experimental timeline. Mice received injections of AAV carrying jRGECO1a (AAV9-Syn.NES-jRGECO1a) at P1-2, underwent cranial window installation at P8-9, and were subsequently imaged from P11 to P21. (B) Representative bright field images showing the cranial window implanted at P9, which remained optically transparent throughout the study. A, anterior; P, posterior; M, midline; L, lateral. (C) Example raster

plots of spontaneous neuronal activity. (D) Event frequency of L2/3 and L4 neurons. (E) Upper panel: raster plot of L2/3 neurons from a P11 female pup. Lower panel: cumulative fraction of active neurons over time corresponding to the upper panel. Synchronous events were identified when the fraction of recruited neurons exceeded the threshold. (F) Frequency of synchronous events in L2/3 and L4 neurons. Numbers of experimental mice. P11, 14 female (F), 20 male (M); P21, 6F, 11M.

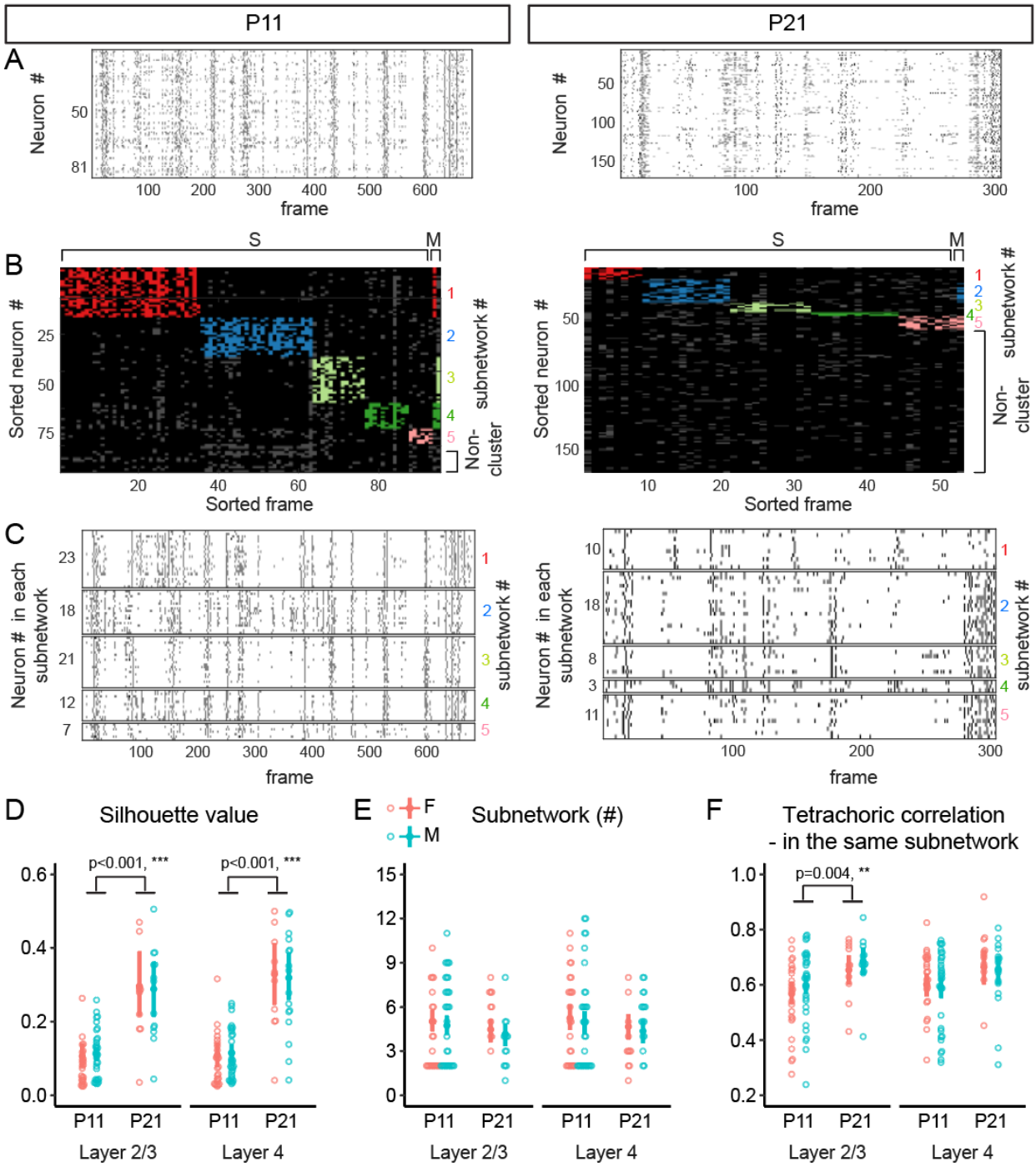

Fig. 2. Developmental increase in subnetwork coherence.

(A) Raster plots showing spontaneous neuronal activity during quiescence at P11 (left) and P21 (right). (B) Re-sorted raster maps based on neuronal subnetwork (y-axis) and event cluster (x-axis). Five distinct neuronal subnetworks (color-coded) were identified at P11 and P21 after assigning neurons to the event clusters in which they participated the

most. Abbreviations: S, events associated with a single event cluster; M, events associated with multiple event clusters. Event clusters without significant neuronal participation were excluded. (C) Raster plots of neurons within each identified subnetwork, with neurons grouped according to their subnetwork identities (color-coded numbers). (D) Silhouette value of event cluster. (E) Number of neuronal subnetworks. (F) Tetrachoric correlation coefficient of neuronal pair within the same subnetwork. Numbers of experimental mice. P11, 14F, 20 M; P21, 6F, 10M.

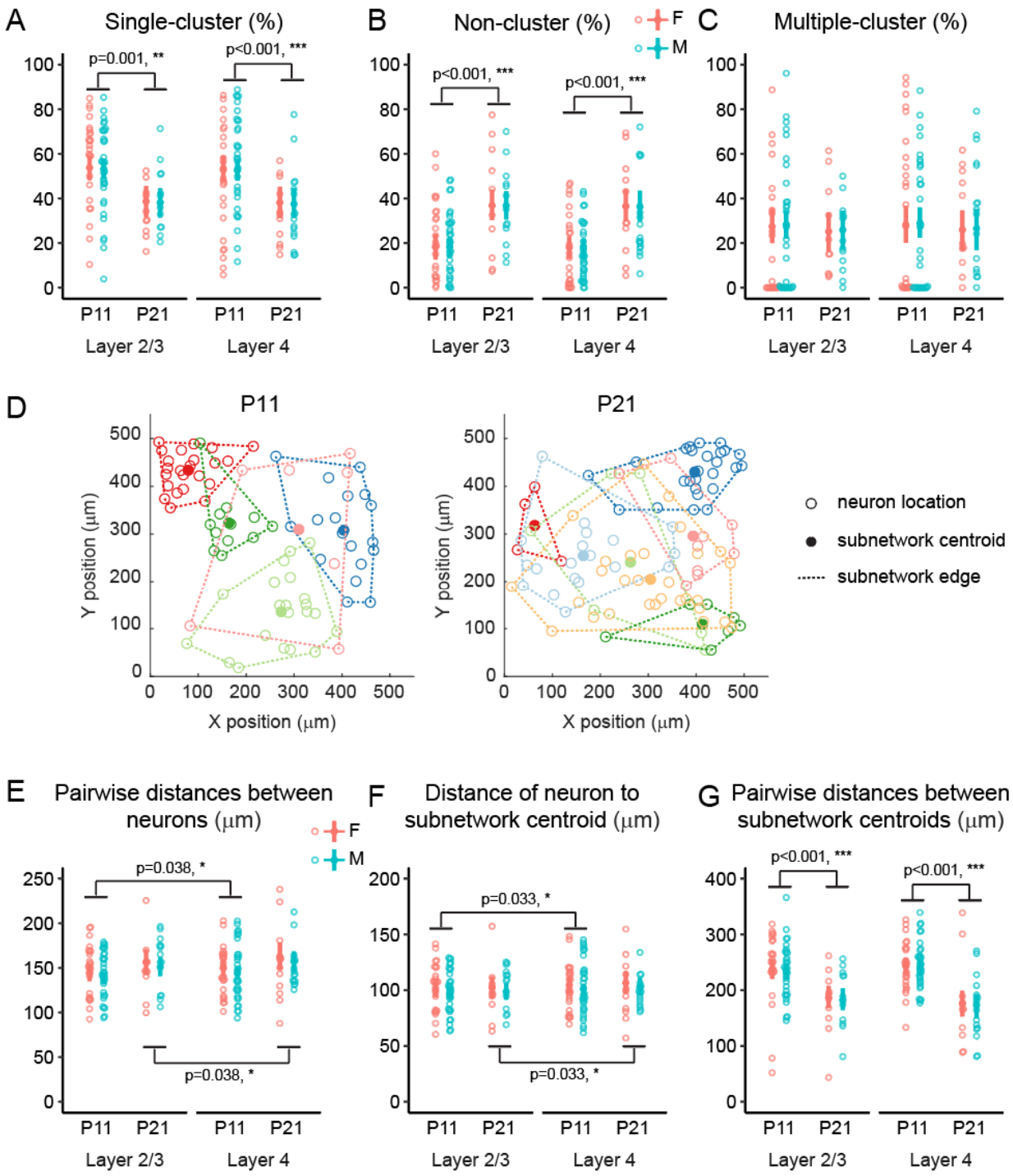

Fig. 3. Subnetwork configuration and topographical distribution.

(A) Percentage of neurons participating in single event clusters. (B) Percentage of neurons not participating in any event cluster. (C) Percentage of neurons participating in multiple event clusters. (D) Neuronal topographical map showing the distribution of neurons within

each subnetwork (color-coded). Open circles represent the locations of individual neurons, while filled circles represent the centroids of the corresponding subnetworks. The subnetwork edges, estimated using the convex hull method, are indicated by dashed lines. Neurons not grouped into subnetworks are not plotted. (E) Pairwise distances among neurons within the same subnetwork. (F) Distances of neurons to their respective subnetwork centroids. (G) Pairwise distances between subnetwork centroids. Animal numbers are the same as in Fig. 2.

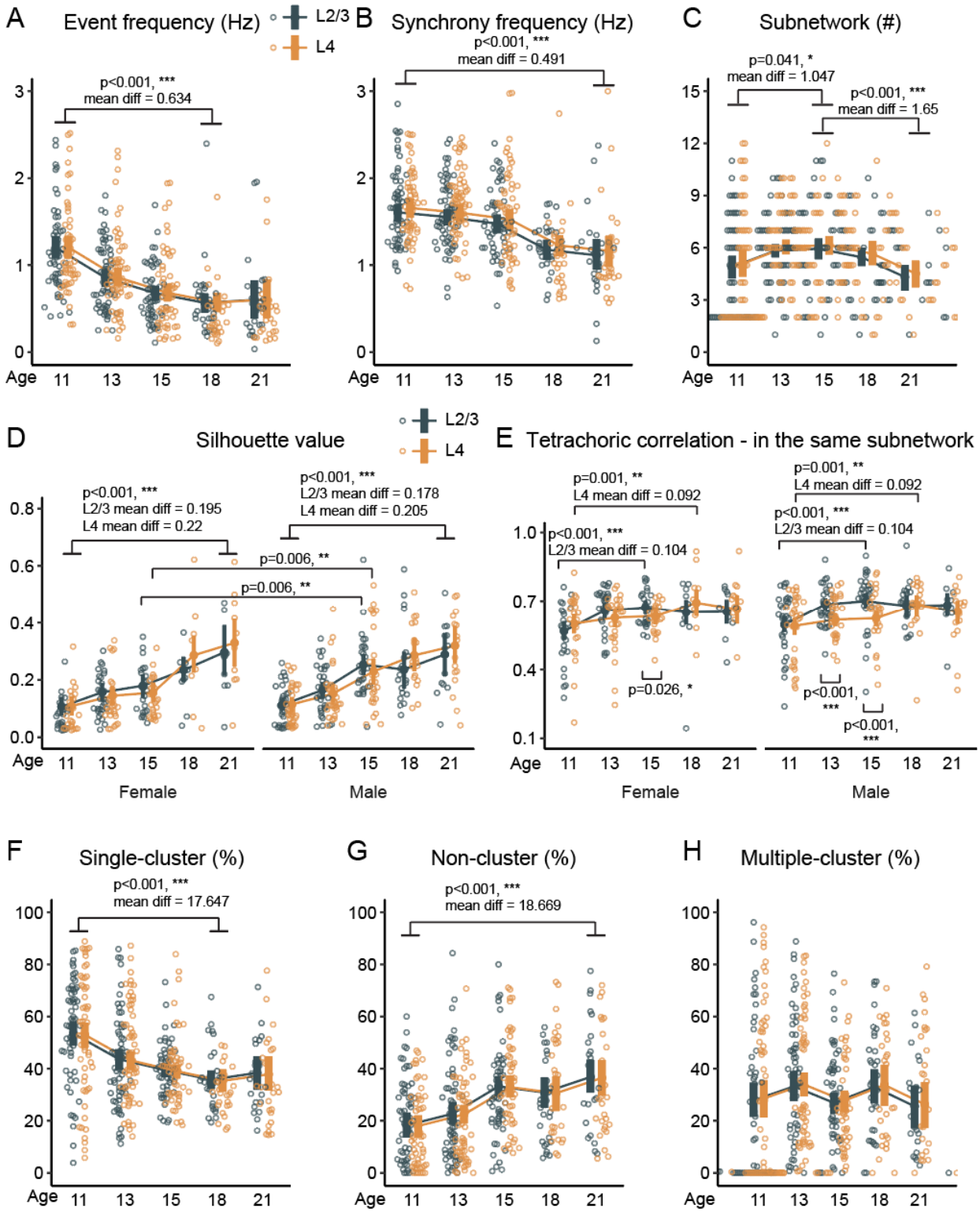

Fig. 4. Developmental trajectory of cortical subnetwork assembly during early postnatal stages. This figure summarizes the progression of various parameters associated with cortical subnetwork development from P11 to P21. (A) Event frequency. (B) Synchrony frequency. (C) Subnetwork number. (D) silhouette value of event clusters. (E) Tetrachoric correlation of neurons within the same subnetwork. (F) Percentage of neurons

976 participating in a single event cluster. (G) Percentage of neurons not involved in any event
977 cluster. (H) Percentage of neurons participating in multiple clusters. Data from both sexes
978 were combined in panels where no sex-dependent effects were observed to streamline the
979 presentation. The age groups with the largest mean differences are annotated to emphasize
980 key developmental transitions. The same animals were used for all figures, and datasets
981 not identified by the K-means clustering algorithm as part of a subnetwork were excluded
982 from the subnetwork-based analysis. Numbers of experimental mice: P11, 14 female (F),
983 20 male (M); P13, 13F, 18M; P15, 11F, 17M; P18, 5F, 11M; P21, 6F, 11M.

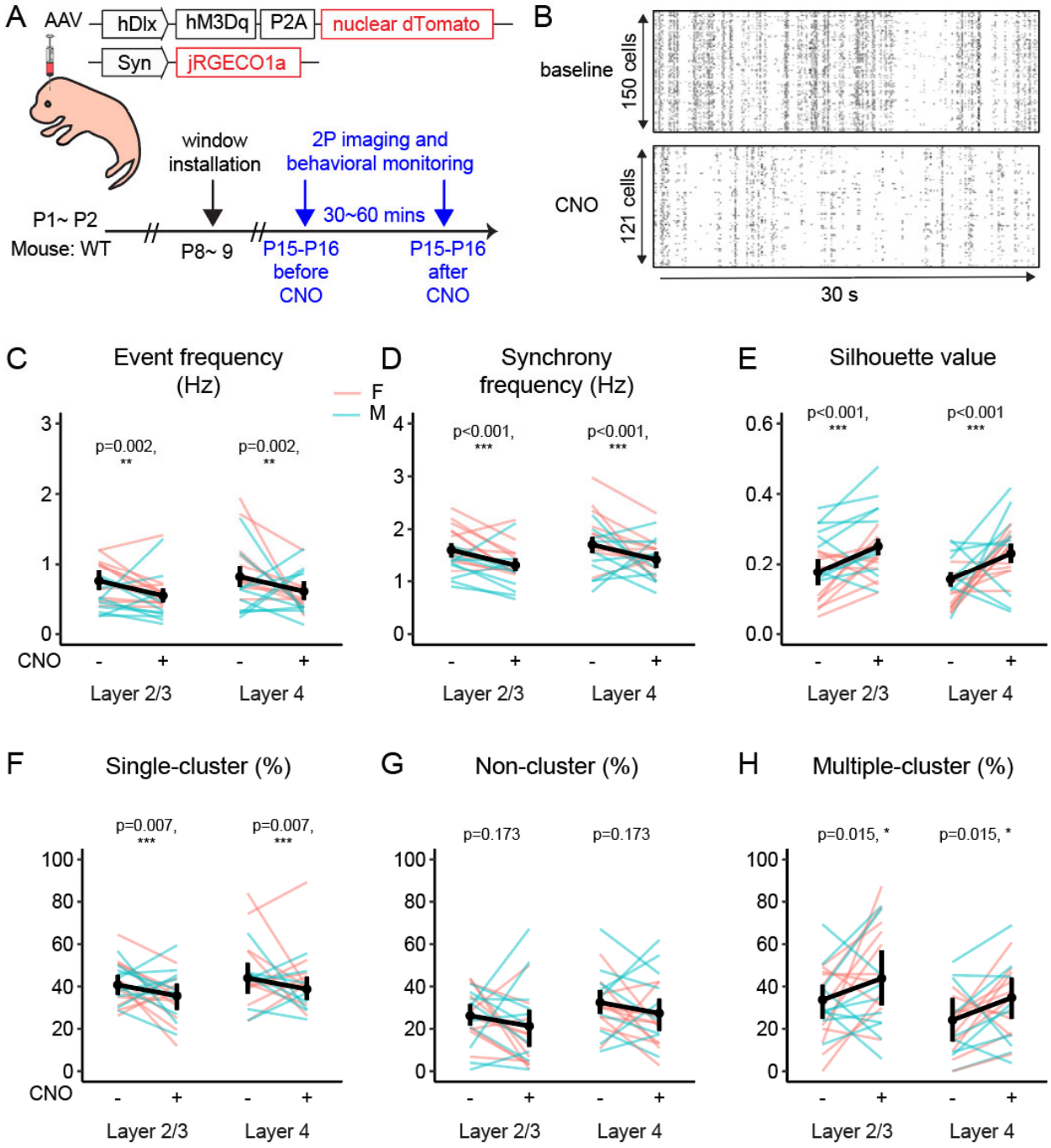

Fig. 5. Enhancing GABAergic transmission reduced glutamatergic neuronal activity and enhanced subnetwork coherence.

(A) The diagram illustrates the experimental design. Mice were co-injected with AAV-carrying jRGECO1a (AAV9-Syn.NES-jRGECO1a) and excitatory DREADD (AAV9-hDlx-hM3Dq-P2A-nuclear dTomato) at P1~2. Following cranial window installation at P8~9, pups were imaged at P15~16. Imaging was performed both before and 30 minutes after the administration of CNO (1 mg/Kg). (B) Raster plot of spontaneous activity of

L2/3 neurons before and after CNO administration. (C) Event frequency. (D) Synchrony frequency. (E) Silhouette value of event cluster. (F) Percentage of neurons participating in a single event cluster. (G) Percentage of neurons not involved in any event cluster. (H) Percentage of neurons participating in multiple clusters. Numbers of experimental mice: 6F, 4M.